



Article

The Effect of Microstructure on Local Corrosion Product Formation during Initial SO₂-Induced Atmospheric Corrosion of ZnAlMg Coating Studied by FTIR-ATR FPA Chemical Imaging

Dan Persson ^{1,*}, Dominique Thierry ¹  and Nathalie LeBozec ^{2,*}

¹ Division of Materials and Production, RISE Research Institutes of Sweden, 16407 Kista, Sweden; dominique.thierry@ri.se

² Institut de la Corrosion/French Corrosion Institute, F-29200 Brest, France

* Correspondence: dan.persson@ri.se (D.P.); nathalie.lebozec@institut-corrosion.fr (N.L.)

Abstract: The initial atmospheric corrosion of ZM (ZnAlMg)-coated steel in humid air (85% RH) and humid argon (85% RH) containing 320 ppb SO₂ was studied using in situ infrared reflection absorption spectroscopy (IRRAS), FTIR-ATR focal plane array (FPA) imaging and SEM-EDS. The corrosion products formed in humid air containing SO₂ are mainly composed of magnesium sulphites and sulphates, with sulphite-containing corrosion products formed initially while the contribution from sulphates increased with exposure time. The results from FTIR-FPA imaging and SEM-EDS showed that the magnesium sulphite and sulphate are formed mainly on eutectic phases with a higher quantity of corrosion products formed on the binary eutectic (Zn-MgZn₂) phases. This is due to presence of microgalvanic elements with the zinc-rich phases as the main sites for the cathodic oxygen reduction while the anodic reactions take place on the eutectic areas. Sulphate content is the highest on the binary eutectic phases, due to the microgalvanic effects and the production of oxidants by the cathodic reaction, which increases the oxidation of sulphite to sulphate.

Keywords: atmospheric corrosion; FTIR-FPA chemical imaging; infrared reflection absorption spectroscopy; SO₂; ZnAlMg-coated steel



Citation: Persson, D.; Thierry, D.; LeBozec, N. The Effect of Microstructure on Local Corrosion Product Formation during Initial SO₂-Induced Atmospheric Corrosion of ZnAlMg Coating Studied by FTIR-ATR FPA Chemical Imaging. *Corros. Mater. Degrad.* **2023**, *4*, 503–515. <https://doi.org/10.3390/cmd4030026>

Academic Editor: Markus Valtiner

Received: 30 June 2023

Revised: 29 August 2023

Accepted: 30 August 2023

Published: 8 September 2023



Copyright: © 2023 by the authors. Licensee MDPI, Basel, Switzerland. This article is an open access article distributed under the terms and conditions of the Creative Commons Attribution (CC BY) license (<https://creativecommons.org/licenses/by/4.0/>).

1. Introduction

Hot-dipped zinc-coated steel alloyed with small amounts of aluminium (from 1 to 4 wt.%) and magnesium (from 1 to 4 wt.%) have been introduced during the last decade as an alternative to conventional hot-dipped galvanised steel (HDG). The alloyed zinc coatings have improved properties compared to classical HDG, such as improved formability and better corrosion resistance. ZnAlMg coatings show better corrosion properties than hot-dipped galvanised steel and zinc-electroplated steel in continuous neutral salt spray (ISO 9227), cyclic corrosion testing, and during various field exposures [1–9]. The atmospheric corrosion rates of Zn₂Al₂Mg-coated steel were two to three times lower than hot-dipped galvanised steel after worldwide exposure in different climate conditions [9]. Zinc aluminium magnesium alloy coatings have a multiphase structure containing primary zinc dendrites and eutectic phases with higher magnesium or aluminium content, as well as a small number of aluminium-rich phases [2,10]. An optical image of a polished and etched surface of Zn₂Al₂Mg is shown in Figure 1.

Corrosion attack on the Zn₂Al₂Mg-coated steel during the atmospheric corrosion after exposure in different outdoor environments was generally localised and occurred preferentially at the eutectic phases of the coating, while the zinc-rich phases to a large extent had not been attacked after 4 years of exposure [9]. Furthermore, compared to HDG, relatively more sulphate-containing products were formed on Zn₂Al₂Mg. An investigation

of the effect of microstructure on atmospheric corrosion in a marine atmosphere indicated that fine microstructures enriched in eutectic phases were more corrosion-resistant than coarser microstructures [11]. This effect was attributed to smaller cathodic zinc-rich phase areas and the preferential dissolution of the eutectic Mg-rich phase, with the subsequent formation of stable layered double hydroxides at the surface. Vint et al. [12] studied the initial corrosion of ZnAlMg and showed that it initiates preferentially within the MgZn_2 lamella within the eutectic phase. It thereafter spreads laterally over the ZM surface preferentially following the MgZn_2 -rich phases with a higher lateral spreading rate for finer microstructures. Using in situ time-lapse microscopy, Sullivan et al. [13] found that corrosion of Zn-(1-2%wt.%)Mg(1-2%wt.%)Al alloys in 0.1% NaCl was initiated in the binary and ternary eutectic regions, with preferential de-alloying of MgZn_2 lamellae.

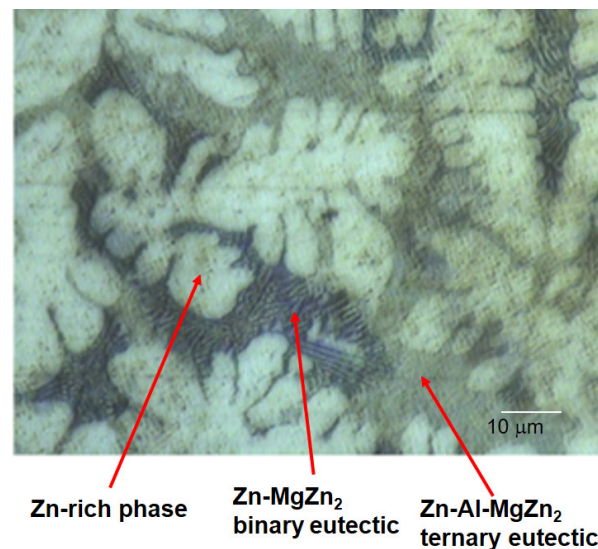


Figure 1. Optical image of polished ZnAlMg-coated steel after etching in picric acid solution.

It should also be noted that the contribution from sulphate-containing corrosion products generally is higher on ZnAlMg compared to HDG and Zn after field exposure [4,5,9,11]. For ZnAlMg exposed in regions of extremely cold and industrial climate [14], Gu et al. observed differences in upward and backward content of sulphur-containing corrosion products, which was explained by dissolution of soluble magnesium sulphates and sulphites by rain and snowfall on the upward side.

It is well known that zinc and zinc-coated steel have high content of sulphur-containing corrosion products [15–19] after exposure in industrial and urban atmosphere, which often is linked to high levels of SO_2 . Laboratory exposures of zinc surfaces in humid air containing SO_2 under well controlled conditions have shown that formation of sulphate is low or absent [20–23]. It is known that the oxidation of S(IV) in the atmosphere is slow in the absence of oxidants and catalysts [24], but that sulphite (SO_3^{2-}) is effectively oxidised in the liquid phase in the atmosphere by hydrogen peroxide and ozone [15,24].

In a previous study, the initial atmospheric corrosion of $\text{Zn}_2\text{Al}_2\text{Mg}$ in humid air containing SO_2 was assessed [23]. Infrared reflection absorption spectroscopy (IRRAS) measurements showed that hydrated magnesium sulphite- and sulphate (SO_4^{2-})-containing corrosion products were formed on the surface of $\text{Zn}_2\text{Al}_2\text{Mg}$. The rate of formation of sulphite- and sulphate-containing corrosion products was much higher than that of pure zinc but comparable to pure magnesium, although only sulphite was formed on pure magnesium. The rapid formation of sulphate-containing corrosion products was attributed to the presence of microgalvanic cells on the alloy surface, where zinc-rich phases were suggested to be sites for the cathodic oxygen reduction reaction, whereas anodic dissolution occurs at adjacent magnesium-rich phases on the surface.

Chemical imaging with Fourier-transform infrared (FT-IR) spectroscopy using focal plane array (FPA) detectors combines chemical specificity from the IR spectra with laterally resolved chemical images of samples. With the FPA detectors, spectra are obtained from all pixels simultaneously, in contrast to a single-element detector, which is scanned over the desired area (mapping). FTIR-FPA imaging has several advantages, including rapid imaging of surface and improved lateral resolution compared to conventional point-to-point FTIR-microscopy mapping. A lateral resolution approaching the diffraction limit, a few microns, is possible with FTIR-FPA measurements using an attenuated total reflectance (ATR) objective. However, the technique is seldomly employed in corrosion studies despite the potential to provide chemical information with relatively high lateral resolution. To our knowledge, FTIR spectrochemical imaging has not yet been applied for studies aiming to relate the chemical composition of corrosion products to the microstructural composition of metal alloys.

The aim of the present study was to better understand the role of different components in the microstructure during initial atmospheric corrosion in SO₂-containing humid air using FTIR-ATR FPA imaging, which provides unique high-resolution chemical imaging in the micrometre range of the initial corrosion product formation and the possibility of distinguishing different chemical forms of sulphur–oxygen compounds locally on the surface. Complementary macroscopic in situ IRRAS measurements also provide time-resolved measurements of the kinetics of formation of corrosion products.

2. Materials and Methods

2.1. Materials

Zn₂Al₂Mg-coated steel containing 2 wt.% aluminium and magnesium was used in this study. The ZnAl₂Mg₂-coated steel has a microstructure with several phases: Zn dendrites, a Zn-MgZn₂ binary eutectic, zones of ternary eutectic Zn-Al-MgZn₂, and Al-dendrites as reported earlier [23,25]. The optical image of a Zn₂Al₂Mg-coating surface polished to #4000 mesh and etched in alcoholic picric acid solution (1 g picric acid and 5 mL HCl and 100 mL ethanol) is presented in Figure 1. The image shows the white dendritic zinc-rich phase, the lamellar binary eutectic phases with a blueish appearance after etching and the ternary eutectic Zn-Al-MgZn₂ as light dark areas. The ZnAlMg-coated steel material was cut into samples with a size of 19 × 22 mm and then sequentially polished with SiC paper to #4000 mesh and rinsed in ethanol before being mounted in the in situ IRRAS cell.

2.2. Exposure Conditions

The corrosive exposures were performed in humid air or humid argon (99.999%) at 85% RH containing 320 ppb SO₂ and <2 ppm CO₂ in a setup for in situ IRRAS measurements described in previous publications [23,25]. All exposures were performed with humid air or humid Ar flowing over the sample with a flow rate of the gas mixture of 1 L/min. The duration of the in situ IRRAS exposures was 3.5 or 16 h. This SO₂ level is in the same order of magnitude as for some severely polluted sites, but considerably higher than the current SO₂ concentrations in Europe or North America [9].

2.3. In Situ Infrared Reflection Absorption Spectroscopy (IRRAS)

In situ infrared reflection absorption spectroscopy (IRRAS) was performed using a Bruker Vertex 70 spectrometer (Bruker Optics, Ettlingen, Germany) and the SeagullTM variable angle reflection accessory (Harrick Scientific Products, Pleasantville, NY, USA). A thermoelectric cooled deuterated alanine doped tri-glycine sulphate (DLATGS) and broadband KBr beam splitter was used during the IRRAS-measurements. The in situ IRRAS measurements were performed at a 78° angle of incidence using a stainless steel exposure cell with KRS-5 windows [23,25]. IRRAS spectra were measured in the region 400 to 4000 cm⁻¹ using p-polarised light and a spectral resolution of 8 cm⁻¹. The in situ IRRAS spectra were recorded with a 30 min interval.

2.4. FTIR-FPA Imaging

Ex-situ Fourier-transform infrared spectroscopy (FTIR) focal plane array (FPA) detector imaging was performed using a Bruker Vertex 70 spectrometer with a Hyperion 3000 microscope (Bruker Optics, Ettlingen, Germany) equipped with a 64×64 FPA detector. The FTIR-FPA imaging was performed using in the attenuated total reflectance (ATR) mode with $20\times$ ATR objective equipped with a $100\ \mu\text{m}$ diameter Ge internal reflection element. The field view is $\approx 33 \times 33\ \mu\text{m}^2$ using the Ge-ATR objective corresponding to a pixel resolution of $\approx 0.5\ \mu\text{m}$. Spectra were acquired in the region 880 to $3860\ \text{cm}^{-1}$ by adding 500 scans at $8\ \text{cm}^{-1}$ resolution. Optical images and optical time-lapse photography were performed with the FTIR microscope. In situ time-lapse imaging was performed in flowing the SO_2 -containing humid air using a modified infrared transmission cell, where one of the windows was replaced with a polished ZnAlMg-coated steel sample.

2.5. SEM-EDS

The FEG-SEM equipment used in this work was a LEO 1530 (Carl Zeiss Microscopy, Jena, Germany) with Gemini column, upgraded to a Zeiss Supra 55 (Carl Zeiss Microscopy, Jena, Germany). The EDS detector was a $50\ \text{mm}^2$ X-Max Silicon Drift Detector (SDD) from Oxford Instruments (Oxford Instruments, Abingdon, UK).

3. Results and Discussion

3.1. In Situ Infrared Reflection Absorption Spectroscopy (IRRAS)

In situ IRRAS spectra obtained during exposure of the polished ZnAlMg-coated steel to humid air and humid argon with 85% RH containing 320 ppb SO_2 after 3.5 h and 16 h are shown in Figures 2 and 3, respectively. The spectra obtained after 3.5 h exposure show bands in the region 3000 to $3700\ \text{cm}^{-1}$ due to the stretching vibrations of water and bending vibrations from water molecules around $1670\ \text{cm}^{-1}$. Both spectra have a strong band at $990\ \text{cm}^{-1}$, which is due to asymmetric stretching vibrations of sulphite ions [23]. These originate from the hydrolysis of SO_2 in the thin water adlayer on the metal surface [15,23]. As discussed in a previous paper, the solvation of SO_2 in the thin water layer can lead to the initial dissolution of surface oxides on the metal surface to the formation of metal sulphite on the surface [23]. For ZnAlMg surface exposed in SO_2 -containing air, a band at $1120\ \text{cm}^{-1}$ due to the asymmetric stretching vibration of the sulphate is clearly present already after 3.5 h exposure and is of similar magnitude to the sulphite band after 16 h exposure. As depicted in Figure 3, only a weak shoulder at $1120\ \text{cm}^{-1}$ due to the sulphate ions is observed after 16 h exposure during exposure in humid argon. Thus, during exposure in humid air the band due to sulphate ions grow much faster compared to the sulphite band. The sulphate is formed by oxidation of sulphite ions in the thin adsorbed water layer at the surface. The intensities of the bands due to sulphite and sulphate are shown in Figure 4 for exposures in humid air and humid argon containing 320 ppb SO_2 . The kinetics of the formation of sulphite and sulphate differ considerably, with sulphite forming very rapidly during the initial hours of exposure, but after a few hours its rate of formation decreased. The formation of sulphate was lower compared to sulphite, but increased steadily with time and reached similar IR intensities as the sulphite band after about 16 h of exposure. The kinetics of the formation of sulphite and sulphate are in qualitative agreement with the previous work [23]. However, in this work, the IR bands due to sulphate were relatively lower than sulphite where polished coating surfaces were used, while the previous work was performed on as-received, skin-passed ZnAlMg coatings.

As shown in a previous work, the formation of sulphate is strongly increased on ZnAlMg-coated steel compared to pure zinc [23]. Sulphite- and sulphate-containing corrosion products enriched in magnesium were formed during exposure in humid air containing SO_2 . The rate of formation of sulphate increased strongly after an initial induction period with lower rate of formation. As seen in Figure 4, the sulphate band is only seen as a weaker shoulder with a low intensity in the spectra for exposure in humid argon, since the oxidation rate of the sulphite apparently is reduced under the oxygen-deficient conditions.

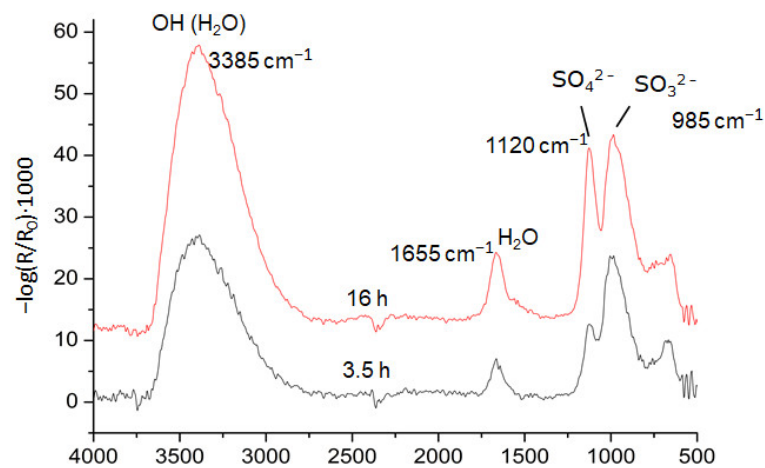


Figure 2. In situ infrared reflection absorption spectra after 3.5 h (black curve) and 16 h (red curve) exposure in humid air (85% RH) containing 320 ppb SO_2 .

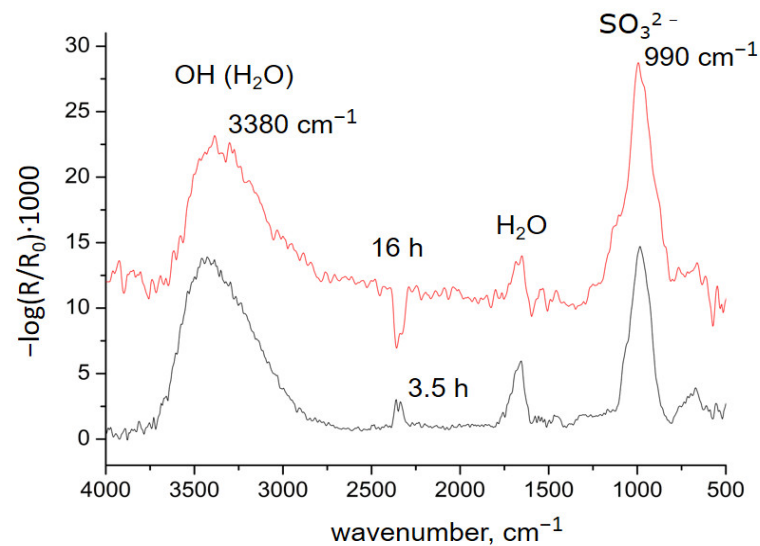


Figure 3. In situ infrared reflection absorption spectra after 3.5 h (black curve) and 16 h (red curve) exposure in humid argon (85% RH) containing 320 ppb SO_2 .

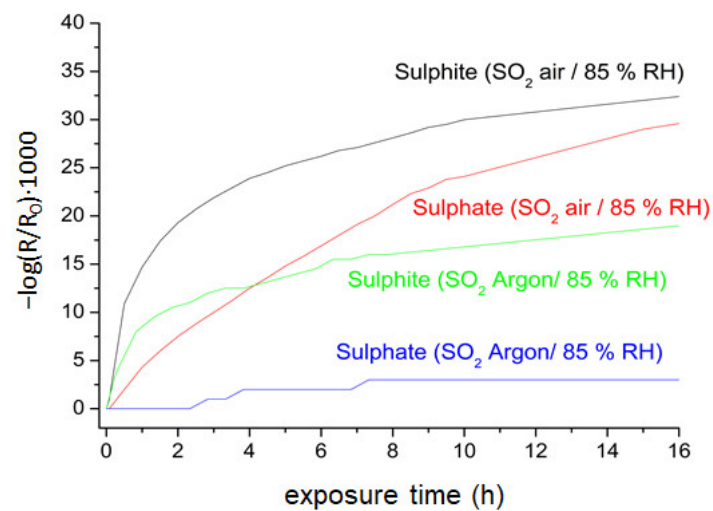


Figure 4. Intensities of sulphite (SO_3^{2-}) and sulphate (SO_4^{2-}) bands for ZnAlMg-coated steel during exposure to humid air or humid argon (85%RH) containing 320 ppb SO_2 .

3.2. FTIR-ATR FPA Imaging and SEM-EDS Measurements

Optical microscopy was used to follow visible changes on the surfaces upon exposure to humid air containing 320 ppb SO₂. Figure 5 shows optical images of polished ZnAlMg after different exposure times. The surface shows a gradual darkening of the eutectic phases with the Zn-MgZn₂ binary eutectics adopting a bluish appearance on the optical images upon prolonged exposures, while the ternary eutectic Zn-Al-MgZn becomes dark yellow/grey.

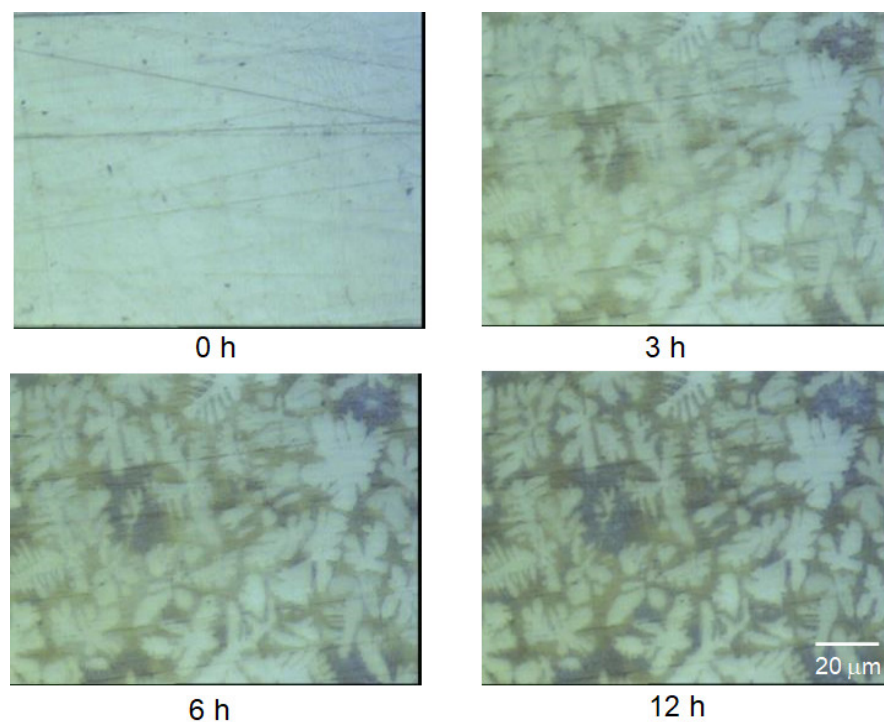


Figure 5. In situ time-lapse optical photographs of ZnAlMg-coated steel during exposure to humid air (85% RH) containing 320 ppb SO₂.

In order to better understand how different microstructural components react during exposure in SO₂-containing atmospheres, FTIR-ATR imaging was performed after 3.5 and 16 h of exposure in humid air with 320 ppb SO₂ and in humid argon containing 320 ppb SO₂ after 16 h. Figure 6 shows a photograph of the polished ZnAlMg-coated steel surface after 3.5 h exposure in humid air with 320 ppb SO₂, together with a false-colour image of the sum of the band areas of the sulphite and sulphate bands at 980 cm⁻¹ and 1100 cm⁻¹, respectively.

The sulphate band is small after short exposure times and is present only as a small shoulder at 1100 cm⁻¹ on the strong sulphite band. The sulphite (and sulphate) is formed almost exclusively on the areas on the surface where the eutectic phases are present. The corrosion product formation leads to a slight darkening of the eutectic phases in the optical images after 3.5 h of exposure, as seen in the photograph in Figure 6. Moreover, the formation of sulphite- and sulphate-containing corrosion products was low on the zinc-rich phases.

After 16 h of exposure, the different eutectic phases are clearly seen in the optical images of the sample, with the binary eutectic having a bluish appearance, as seen in Figure 7. The FTIR-ATR image based on the sum of the integrated areas of the sulphite and sulphate bands shows a preferential formation of sulphite- and sulphate-containing corrosion products on the eutectic phases, while the zinc-rich phases are much less affected. The intensities of the sulphate bands are the highest at the binary eutectic areas and also at areas quite close to the zinc-rich phases.

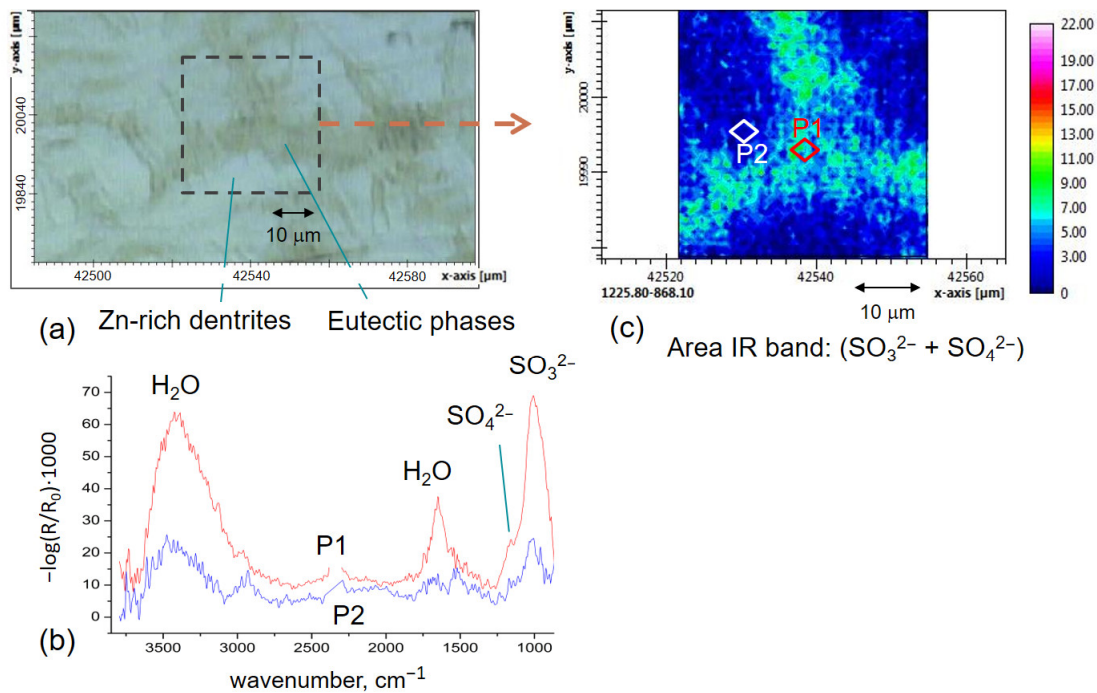


Figure 6. FTIR-ATR FPA imaging of ZnAlMg-coated steel after 3.5 h exposure to humid air (85% RH) containing 320 ppb SO_2 . (a) Optical photographs of surface; (b) FTIR-ATR spectra in areas located on the eutectic (P1) and the zinc-rich dendrite (P2); (c) false-colour image of the area of the IR bands of $\text{SO}_3^{2-} + \text{SO}_4^{2-}$.

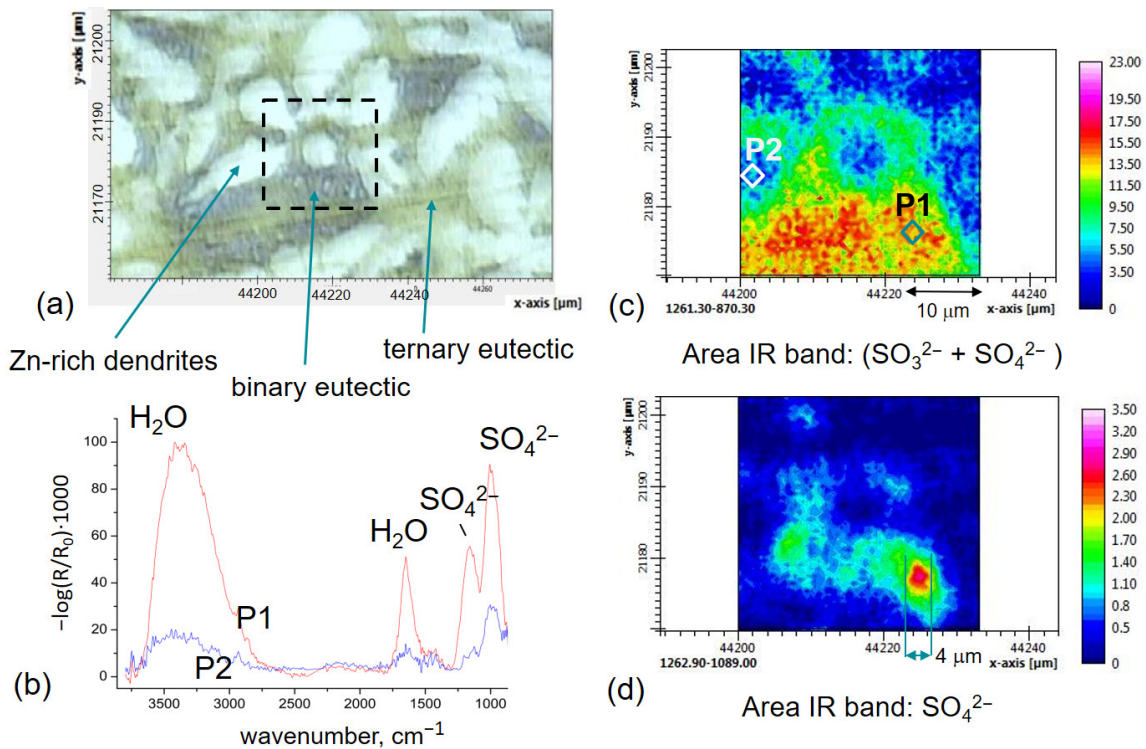


Figure 7. FTIR-ATR FPA imaging on the surface of ZnAlMg-coated steel after 16 h exposure to humid air (85% RH) containing 320 ppb SO_2 . (a) Optical photographs of surface; (b) FTIR-ATR spectra in selected areas located on the binary eutectic (P1) and the zinc-rich dendrite (P2); (c) false-colour image of the area of the IR bands of $\text{SO}_3^{2-} + \text{SO}_4^{2-}$; (d) false-colour image of the area of the IR band of SO_4^{2-} .

For surface exposed in humid Ar containing 320 ppb SO₂, sulphite-containing corrosion products formed preferentially in the eutectic phases as for the exposure in humid air (Figure 8). However, the formation of sulphate is considerably reduced, with only a shoulder around 1100 cm⁻¹ on the strong sulphite band. FTIR-images of the surface after 16 h exposure show that the sulphite (and sulphate) formed nearly exclusively on the eutectic phases also under these conditions, while the intensities of the sulphite/sulphate band are very low on the zinc-rich dendrites. It is plausible that the reduced formation of sulphate during exposure to SO₂ contaminated humid argon is related to the low oxygen content, which can decrease the oxygen reduction rate on the surface. The formation of low amounts of sulphite- and sulphate-containing corrosion products on the zinc-rich phases indicates that these are the sites for the cathodic reactions as in the case of humid air. At reduced oxygen concentrations, the rate of the oxygen reduction reaction on the zinc-rich phases will be lower compared to ambient oxygen content, and less reaction product, which can promote the oxidation of sulphite to sulphate, will be formed. The formation of sulphite corrosion products in oxygen-deficient conditions in humid argon is also reduced compared to exposure in humid air, probably due to an overall decrease in the corrosion rate due to the low oxygen concentration. It is often observed that oxygen reduction determines the corrosion during atmospheric conditions where thin electrolyte layers are present on the surfaces [26–28] However, it cannot be ruled out that water reduction could contribute to the cathodic processes under these circumstances, particularly in areas where the magnesium content is high.

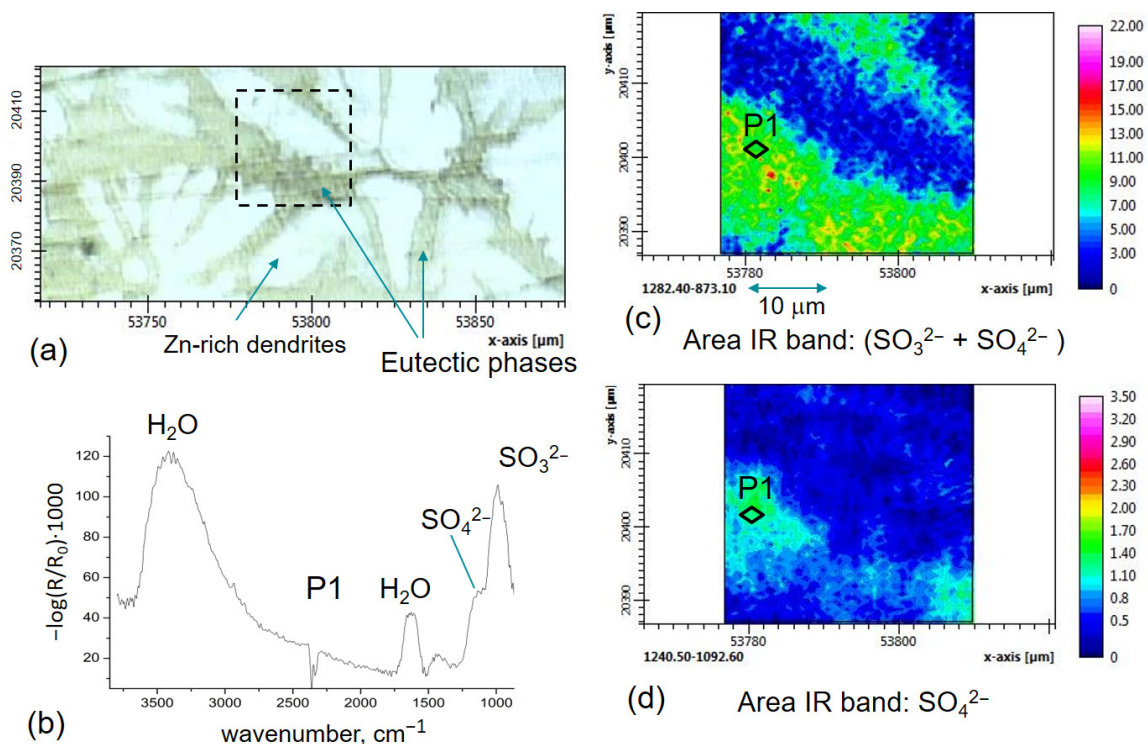


Figure 8. FTIR-ATR FPA imaging of ZnAlMg-coated steel after 16 h exposure to argon (85% RH) containing 320 ppb SO₂. (a) Optical photographs of surface; (b) FTIR-ATR spectra on the eutectic area (P1); (c) false-colour image of the area of the IR bands of SO₃²⁻ + SO₄²⁻; (d) area of the IR band of SO₄²⁻.

Another factor that can promote corrosion in humid air is the formation of hygroscopic/soluble magnesium sulphate salt [29]. Since dissolution of ionic species should decrease water activity in the electrolyte layer, this will lead to more water absorbed in the electrolyte layer on the surface in these locations and increase the local surface elec-

trolyte thickness in the anodic areas. This can further promote the anodic dissolution of the eutectic phases.

The SEM-EDS maps presented in Figure 9 are consistent with the results of the FTIR imaging. These measurements confirm that the formation of sulphur and oxygen corrosion products is observed to occur preferably on the Mg-rich phases on the surface. Co-located spots with a higher content of O and S are seen on the Mg-rich areas adjacent to the Zn dendrites. These spots of a few microns in size probably correspond to the areas with higher sulphate content seen in the FTIR-images in Figure 7.

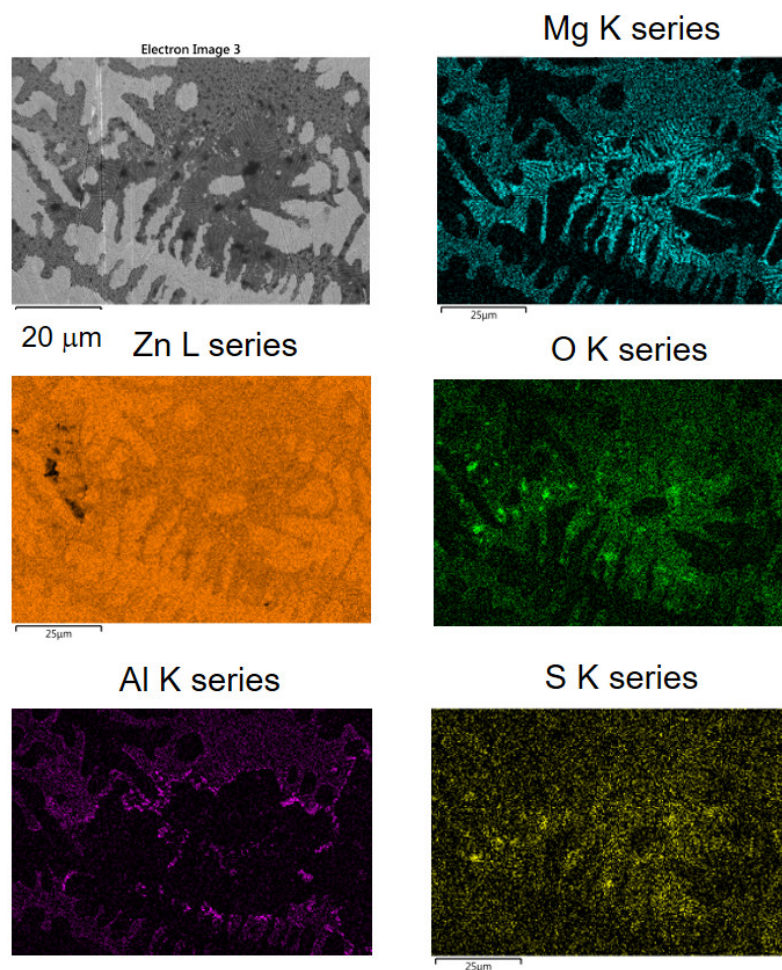


Figure 9. SEM-EDS maps of ZnAlMg-coated steel after 16 h exposure to humid air (85% RH) containing 320 ppb SO_2 (magnification $\times 1200$).

The in situ IRRAS measurements and microscopic imaging performed by FTIR-ATR FPA imaging and SEM-EDS convey a concise view of the interaction of SO_2 -polluted humid air with a ZnAlMg surface. The atmospheric corrosion in SO_2 -containing humid air leads to a preferential attack on the eutectic phases with the formation of sulphite- and sulphate-containing corrosion products on these phases. High amounts of sulphate-containing corrosion product are formed locally on the Mg-rich binary eutectic phase. During initial exposure, SO_2 dissolved in the water adlayer can lead to a slight acidification of the aqueous layer [30], which can lead to dissolution of surface oxides and the subsequent formation of metal-sulphite complexes and sulphite-containing surface films. After prolonged exposure, oxidation of sulphite to sulphate is taking place. We suggest that a crucial role is played by the formation of microgalvanic elements on the surface with zinc-rich dendritic phases as sites for the cathodic reaction(s) and the eutectic anodic sites. Oxidation of sulphite to sulphate can be enhanced due to the presence of oxidants, such as peroxide or super-

oxide formed by the cathodic oxygen reduction reaction. The oxygen reduction on zinc in oxygen saturated sulphate solutions in the pH range 4–11 was studied by Boto and Williams [31], and it was found that a mixture of H₂O₂ and hydroxide was formed. In a study [32] performed on bare and passive zinc, it was observed that hydroperoxyl ions are produced on passive zinc, while the reaction proceeds primarily by a direct four-electron reduction to hydroxyl ions on bare zinc. By in situ and operando attenuated total reflection infrared (ATR-IR) spectroscopy Nayak et al. [33] detected surface-bound superoxide during the oxygen reduction reaction (ORR) on electrodeposited zinc hydroxide-based model corrosion products.

Since small amounts of corrosion products are formed on the cathodic zinc-rich phases and soluble magnesium sulphate/sulphite are formed on the eutectics, and in particular the binary eutectic, the cathodic and anodic sites are separated and the corrosion can propagate easily without blocking the cathodic areas by corrosion products. Due to the separation of the anodic and cathodic areas, differences in pH values can be maintained on the surface that favour the formation of more soluble corrosion products in the anodic areas. On the other hand, uptake of SO₂ is facilitated by a higher pH, which should prevail at and close to the cathodic areas. Formation of soluble reaction products such as magnesium sulphate [29] also promotes increased water uptake on the surface. Since the formation of corrosion product is low on the zinc-rich dendrites, the cathodic reaction can maintain a high reaction rate without being blocked at the surface. However, formation of large amounts of corrosion products in the anodic areas will eventually limit the anodic process.

An alternative mechanism is that the eutectic phases corrode preferentially with both the anodic and cathodic processes occurring in close proximity on the lamellar microstructure on these. The binary eutectic consists of a Zn-MgZn₂ lamellar microstructure, and sites for the cathodic reactions could be the Zn-rich phase, while the anodic dissolution would occur on MgZn₂. However, the formation of corrosion products on the binary eutectic could block sites for cathodic reaction, which could rapidly decrease the corrosion rate, since these anodic and cathodic areas are very close in this case.

It has been found that the oxidation of SO₂ by hydrogen peroxide decreases with increasing pH [34], which should lead to higher oxidation rate of sulphite closer to anodic areas, where a lower pH is expected. The sulphite ions formed in connection with the cathodic areas are transported towards the anodic areas in the eutectic phases. As observed by FTIR-imaging, the formation of sulphate was highest in the binary eutectic areas, where hydroxyl ions can be produced by the cathodic reaction on zinc-rich areas in the eutectic or zinc-rich phases in proximity to the eutectic. The location of the areas with high sulphate formation is probably linked to local pH differences on the surface.

Dissolution of SO₂ in the thin adlayer of water on the surface leads to the formation of sulphite ions:



In the eutectic areas, dissolution of magnesium takes place at the surface during the propagation of the corrosion:



Sites for the cathodic oxygen reduction reaction are the zinc-rich phases on the surface.



The oxygen reaction often takes place in two steps, with the formation of intermediates, such as peroxide and superoxide [31–33,35,36]. The formation of such oxidants will facilitate and increase the rate of oxidation of sulphite to sulphate:



The oxidation of sulphite in aqueous solutions is very low in the absence of catalysts and oxidant. In liquid water in the atmosphere as clouds, fog, and rain, H₂O₂ is believed to

be one of the most important oxidizers of sulphite, while some metal ions such as Fe(III) and Mn(II) are efficient catalysts for the oxidation [24]. It cannot be ruled out that small amount of Fe is present in the ZnAlMg coating and may contribute to the formation of sulphate in anodic areas, where Fe might be dissolved.

At the anodic areas in the eutectics, Mg ions are precipitated as hydrated magnesium sulphate/sulphite:

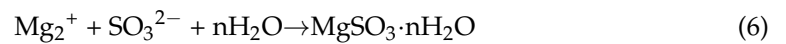
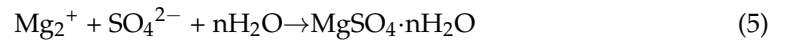


Figure 10 shows schematically the mechanism of propagation of the corrosion of ZnAlMg in humid air containing SO_2 with preferential corrosion on the eutectic phases on the surface.

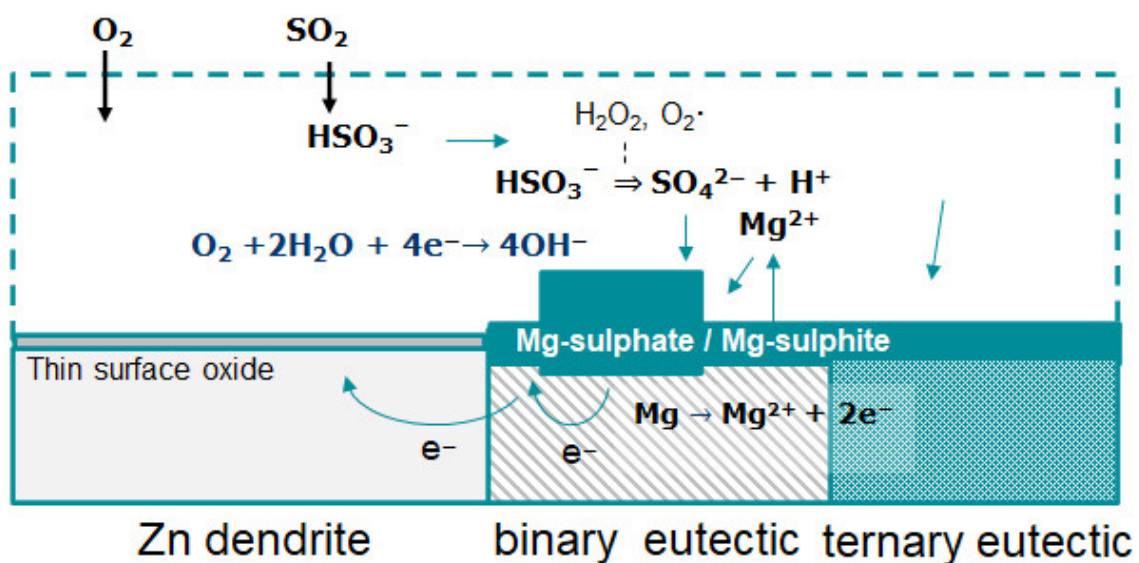


Figure 10. Schematic description of initial atmospheric corrosion of ZnAlMg in humid air containing SO_2 .

4. Conclusions

The initial atmospheric corrosion of ZnAlMg-coated steel surfaces in SO_2 -containing humid air was studied using in situ IRRAS, FTIR-ATR FPA chemical imaging and SEM-EDS. Using FTIR-FPA imaging information about the distribution and composition of corrosion products was obtained from early stages of corrosion under atmospheric conditions and how the initial corrosion product formation was related to the microstructure of the ZnAlMg coating.

During exposure to humid air containing SO_2 , $\text{MgSO}_x \cdot n\text{H}_2\text{O}$ corrosion products were formed. Initially, the formation of sulphite-containing corrosion products was high, but after prolonged exposures, the contribution of sulphate increased. Exposures in humid argon resulted in the reduction in the formation of sulphate on the surfaces due to the lower oxygen content.

With FTIR-FPA imaging, it was shown that sulphite- and sulphate-containing corrosion products were formed almost exclusively on eutectic phases, while the zinc-rich dendrites were largely unaffected. The chemical imaging showed that the highest amount of corrosion products was formed on the binary eutectic (Zn-MgZn_2) phases and also the highest sulphate content was seen in the binary eutectic phases.

Oxidation of sulphite to sulphate is probably facilitated by the formation of intermediates in the cathodic process, such as peroxide and superoxide forming during oxygen reduction on zinc and oxidised zinc surfaces on the eutectics or adjacent zinc-rich phases.

In line with that, the formation of sulphate was strongly reduced during exposures in oxygen-deficient conditions in SO₂-containing humid argon.

Author Contributions: Conceptualisation, D.P., D.T. and N.L.; methodology, D.P., D.T. and N.L.; validation, D.P.; formal analysis, D.P.; investigation, D.P.; resources, D.T. and N.L.; data curation, D.P.; writing—original draft preparation, D.P.; writing—review and editing, D.P., D.T. and N.L.; visualisation, D.P.; project administration, D.T. and N.L.; funding acquisition, D.T. and N.L. All authors have read and agreed to the published version of the manuscript.

Funding: This research received no external funding.

Data Availability Statement: The data presented in this study are available on request from the corresponding author.

Acknowledgments: We acknowledge Malin Tornberg for performing SEM-EDS measurements.

Conflicts of Interest: The authors declare no conflict of interest.

References

1. Schürz, S.; Luckeneder, G.H.; Preis, K.; Haunschmied, T.; Mori, G.; Kneissl, A.C. Corrosion behaviour of Zn–Al–Mg coated steel sheet in sodium chloride-containing environment. *Corros. Sci.* **2009**, *51*, 2355–2363. [[CrossRef](#)]
2. Schürz, S.; Luckeneder, G.H.; Fleischanderl, M.; Mack, P.; Gsaller, H.; Kneissl, A.C.; Mori, G. Chemistry of corrosion products on Zn–Al–Mg alloy coated steel. *Corros. Sci.* **2010**, *52*, 3271–3279. [[CrossRef](#)]
3. Prosek, T.; Larché, N.; Vlot, M.; Goodwin, F.; Thierry, D. Corrosion performance of Zn–Al–Mg coatings in open and confined zones in conditions simulating automotive applications. *Mater. Corros.* **2010**, *60*, 412–420. [[CrossRef](#)]
4. Diler, E.; Rouvellou, B.; Rioual, S.; Lescop, B.; Vien, G.N.; Thierry, D. Characterization of corrosion products of Zn and Zn–Mg–Al coated steel in a marine atmosphere. *Corros. Sci.* **2014**, *87*, 111–117. [[CrossRef](#)]
5. Azevedo, M.S.; Allély, C.; Ogle, K.; Volovitch, P. Corrosion mechanisms of Zn (Mg, Al) coated steel in accelerated tests and natural exposure: 1. The role of electrolyte composition in the nature of corrosion products and relative corrosion rate. *Corros. Sci.* **2015**, *90*, 472–481. [[CrossRef](#)]
6. Tomandl, A.; Labrenz, E. The corrosion behavior of ZnAlMg alloys in maritime environments. *Mater. Corros.* **2016**, *67*, 1286–1293. [[CrossRef](#)]
7. Volovitch, P.; Vu, T.N.; Allély, C.; Abdel, A.; Aal, A.A.; Ogle, K. Understanding corrosion via corrosion product characterization: II. Role of alloying elements in improving the corrosion resistance of Zn–Al–Mg coatings on steel. *Corros. Sci.* **2011**, *53*, 2437–2445. [[CrossRef](#)]
8. LeBozec, N.; Thierry, D.; Peltola, A.; Luxem, L.; Luckeneder, G.; Marchiaro, G.; Rohwerder, M. Corrosion performance of Zn–Mg–Al coated steel in accelerated corrosion tests used in the automotive industry and field exposures. *Mater. Corros.* **2013**, *64*, 969–978. [[CrossRef](#)]
9. Thierry, D.; Persson, D.; Luckeneder, G.; Stellnberger, K.-H. Atmospheric corrosion of ZnAlMg coated steel during long term atmospheric weathering at different worldwide exposure sites. *Corros. Sci.* **2019**, *148*, 338–354. [[CrossRef](#)]
10. Duchoslav, J.; Truglas, T.; Groiß, H.; Riener, C.K.; Arndt, M.; Stellnberger, K.H.; Luckeneder, G.; Angeli, G.; Stifter, D. Structure and chemistry of surface oxides on ZnMgAl corrosion protection coatings with varying alloy composition. *Surf. Coat. Tech.* **2019**, *368*, 51–58. [[CrossRef](#)]
11. LeBozec, N.; Thierry, D.; Persson, D.; Riener, C.K.; Luckeneder, G. Influence of microstructure of zinc-aluminium-magnesium alloy coated steel on the corrosion behavior in outdoor marine atmosphere. *Surf. Coat. Technol.* **2019**, *374*, 897–909. [[CrossRef](#)]
12. Wint, N.; Cooze, N.; Searle, J.R.; Sullivan, J.H.; Williams, G.; McMurray, H.N.; Luckeneder, G.; Riener, C.J. The effect of microstructural refinement on the localized corrosion of model Zn–Al–Mg alloy coatings on steel. *Electrochem. Soc.* **2019**, *166*, C3147. [[CrossRef](#)]
13. Sullivan, J.; Mehraban, S.; Elvins, J. In situ monitoring of the microstructural corrosion mechanisms of zinc–magnesium–aluminium alloys using time lapse microscopy. *Corros. Sci.* **2011**, *54*, 2208–2215. [[CrossRef](#)]
14. Gu, T.; Liu, Y.; Zhang, C.P.; Wang, Z. Initial atmospheric corrosion of zinc-aluminum-magnesium coated steel and galvanized steel in regions of extremely cold and industrial climate. *Mat. Chem. Phys.* **2022**, *291*, 126686. [[CrossRef](#)]
15. Graedel, T.E. Corrosion mechanisms for zinc exposed to the atmosphere. *J. Electrochem. Soc.* **1989**, *136*, 193C–203C. [[CrossRef](#)]
16. Zhang, X.G. *Corrosion and Electrochemistry of Zinc*; Springer: New York, NY, USA, 1996.
17. Leygraf, C.; Wallinder, I.O.; Tidblad, J.; Graedel, T. *Atmospheric Corrosion*; John Wiley & Sons: Hoboken, NJ, USA, 2016.
18. De la Fuente, D.; Castano, J.G.; Morcillo, M. Long-term atmospheric corrosion of zinc. *Corros. Sci.* **2007**, *49*, 1420–1436. [[CrossRef](#)]
19. Persson, D.; Thierry, D.; Karlsson, O. Corrosion and corrosion products of hot dipped galvanized steel during long term atmospheric exposure at different sites world-wide. *Corros. Sci.* **2017**, *126*, 152–165. [[CrossRef](#)]
20. Sydberger, T.; Vannerberg, N.G. The influence of the relative humidity and corrosion products on the adsorption of sulfur dioxide on metal surfaces. *Corr. Sci.* **1972**, *12*, 775–784. [[CrossRef](#)]

21. Duncan, J.R.; Spedding, D.J. The effect of relative humidity on adsorption of sulphur dioxide on to metal surfaces. *Corros. Sci.* **1973**, *13*, 993–1001. [[CrossRef](#)]
22. Duncan, J.R.; Spedding, D.J. The mode of initial reaction of SO₂ at a metal surface. *Corros. Sci.* **1974**, *14*, 241–249. [[CrossRef](#)]
23. Persson, D.; LeBozec, T.P.N.; Thierry, D.; Luckeneder, G. Initial SO₂-induced atmospheric corrosion of ZnAlMg coated steel studied with in situ Infrared Reflection Absorption Spectroscopy. *Corros. Sci.* **2015**, *90*, 276–283. [[CrossRef](#)]
24. Martin, L.R. *SO₂, NO and NO₂ Oxidation Mechanisms: Atmospheric Considerations*; Calvert, J.G., Ed.; Butterworth Publishers: Stoneham, MA, USA, 1984.
25. Persson, D.; Thierry, D.; LeBozec, N.; Prosek, T. In situ infrared reflection spectroscopy studies of the initial atmospheric corrosion of Zn–Al–Mg coated steel. *Corros. Sci.* **2013**, *72*, 54–63. [[CrossRef](#)]
26. Ito, M.; Ooi, A.; Tada, E.; Nishikata, A. In situ evaluation of carbon steel corrosion under salt spray test by electrochemical impedance spectroscopy. *J. Electrochem. Soc.* **2020**, *167*, 101508. [[CrossRef](#)]
27. Similion, H.; Dolgikh, O.; Terryn, H.; Deconinck, J. Atmospheric corrosion modeling. *J. Corros. Rev.* **2014**, *32*, 73–100. [[CrossRef](#)]
28. Zhong, X.; Schulz, M.; Wu, C.-H.; Rabe, M.; Erbe, A.; Rohwerder, M. Limiting current density of oxygen reduction under ultrathin electrolyte layers: From the micrometer range to monolayers. *ChemElectroChem* **2021**, *8*, 712–718. [[CrossRef](#)]
29. Steiger, M.; Linnow, K.; Ehrhardt, D.; Rohde, M. Decomposition reactions of magnesium sulfate hydrates and phase equilibria in the MgSO₄–H₂O and Na⁺–Mg₂+–Cl[–]–SO₄^{2–}–H₂O systems with implications for Mars. *Goechim. Cosmochim. Acta* **2011**, *75*, 3600–3626. [[CrossRef](#)]
30. Terraglio, F.P.; Manganelli, R.M. The absorption of atmospheric sulfur dioxide by water solutions. *J. Air Pollut. Control. Assoc.* **1967**, *17*, 403–406. [[CrossRef](#)]
31. Boto, K.G.; Williams, L.F.G. Rotating disc electrode studies of zinc corrosion. *J. Electroanal. Chem.* **1977**, *77*, 1–20. [[CrossRef](#)]
32. Wroblowa, H.S.; Qaderi, S.B. The mechanism of oxygen reduction on zinc. *J. Electroanal. Chem.* **1990**, *295*, 153–161. [[CrossRef](#)]
33. Nayak, S.; Biedermann, P.U.; Erbe, A. Superoxide intermediate in the oxygen reduction on a zinc hydroxide model corrosion product. *J. Chem. Phys.* **2022**, *157*, 224702. [[CrossRef](#)]
34. Hoffmann, M.R.; Edwards, J.O. Kinetics of the oxidation of sulfite by hydrogen peroxide in acidic solution. *J. Phys. Chem.* **1975**, *79*, 2096–2098. [[CrossRef](#)]
35. Dafydd, H.; Worsley, D.A.; McMurray, H.N. The kinetics and mechanism of cathodic oxygen reduction on zinc and zinc–aluminium alloy galvanized coatings. *Corros. Sci.* **2005**, *47*, 3006–3018. [[CrossRef](#)]
36. Yadav, P.; Nishikata, A.; Tsuru, T.J. Oxygen reduction mechanism on corroded zinc. *Electroanal. Chem.* **2005**, *585*, 142–149. [[CrossRef](#)]

Disclaimer/Publisher’s Note: The statements, opinions and data contained in all publications are solely those of the individual author(s) and contributor(s) and not of MDPI and/or the editor(s). MDPI and/or the editor(s) disclaim responsibility for any injury to people or property resulting from any ideas, methods, instructions or products referred to in the content.